Nonlinear estimation-based dipole source localization for artificial lateral line systems

2013 Bioinspir. Biomim. 8 026005

(http://iopscience.iop.org/1748-3190/8/2/026005)

Bioinspir. Biomim. **8** (2013) 026005 (15pp) doi:10.1088/1748-3182/8/2/026005

Nonlinear estimation-based dipole source localization for artificial lateral line systems

Ahmad T Abdulsadda[1,2] **and Xiaobo Tan**[1,3]

[1] Smart Microsystems Laboratory, Department of Electrical and Computer Engineering, Michigan State University, East Lansing, MI 48824, USA
[2] Communication Department, Al Najaf Technical College, Abo Skeer Street, Al Najaf, Iraq

E-mail: abdulsad@msu.edu and xbtan@msu.edu

Received 5 August 2012
Accepted for publication 11 March 2013
Published 28 March 2013
Online at stacks.iop.org/BB/8/026005

Abstract

As a flow-sensing organ, the lateral line system plays an important role in various behaviors of fish. An engineering equivalent of a biological lateral line is of great interest to the navigation and control of underwater robots and vehicles. A vibrating sphere, also known as a dipole source, can emulate the rhythmic movement of fins and body appendages, and has been widely used as a stimulus in the study of biological lateral lines. Dipole source localization has also become a benchmark problem in the development of artificial lateral lines. In this paper we present two novel iterative schemes, referred to as Gauss–Newton (GN) and Newton–Raphson (NR) algorithms, for simultaneously localizing a dipole source and estimating its vibration amplitude and orientation, based on the analytical model for a dipole-generated flow field. The performance of the GN and NR methods is first confirmed with simulation results and the Cramer–Rao bound (CRB) analysis. Experiments are further conducted on an artificial lateral line prototype, consisting of six millimeter-scale ionic polymer–metal composite sensors with intra-sensor spacing optimized with CRB analysis. Consistent with simulation results, the experimental results show that both GN and NR schemes are able to simultaneously estimate the source location, vibration amplitude and orientation with comparable precision. Specifically, the maximum localization error is less than 5% of the body length (BL) when the source is within the distance of one BL. Experimental results have also shown that the proposed schemes are superior to the beamforming method, one of the most competitive approaches reported in literature, in terms of accuracy and computational efficiency.

(Some figures may appear in colour only in the online journal)

1. Introduction

The lateral line system is an important flow-sensing organ for fish [6]. A lateral line comprises arrays of mechanoreceptive units called neuromasts. Each neuromast consists a bundle of sensory hair cells encapsulated in a gelatinous cupula [17] . There are two types of neuromasts, superficial neuromasts that stand on the skin, and canal neuromasts that are located in fluid-filled canals below the skin surface. With distinct dynamic characteristics, superficial neuromasts tend to respond to flow velocities while canal neuromasts respond to flow accelerations (or pressure gradients) [39, 22]. The interaction between the flow and the cupula generates trains of neuronal pulses which are transmitted to the central nervous system for information processing [7, 12, 13]. The lateral line is involved in various behaviors of fish, such as prey/predator detection [33, 50], schooling [49], station holding [8], object detection and avoidance [60, 62], rheotaxis [45, 27], energy-efficient swimming [41], and courtship and communication [13].

An engineering equivalent of a biological lateral line is of great interest to the navigation and control of underwater robots and vehicles. In particular, an artificial lateral line will

[3] Author to whom any correspondence should be addressed.

represent a new, noiseless sensing modality for underwater applications that is complementary to traditional sensors such as vision and sonar [12, 42]. A number of micromachined flow sensors, inspired by neuromasts in fish lateral lines [23, 43, 51, 63] or by wind receptor hairs in insects [21, 47], have been reported in the last decade. These sensors typically have an out-of-plane beam structure that bends or deforms during the interaction with a flow. The bending or deformation, which carries information about the flow, is captured via resistance change [23, 43, 47, 51, 61, 64] or capacitance change [21, 53]. Hair cell-inspired sensors have also been developed at slightly larger scales, exploiting optical transduction [38] or novel sensing materials such as ionic polymer–metal composites (IPMCs) [2, 3] and gel-supported lipid bilayers [54].

Extensive behavioral and neurophysiological studies have been conducted by biologists to understand how hydrodynamic stimuli are encoded and processed in the lateral line system [7, 14–16, 19, 62], which could potentially provide insight into information processing for artificial lateral lines. Theoretical work on flow modeling in the context of lateral lines is often instrumental in both explaining hydrodynamic imaging by fish and guiding the information extraction in artificial lateral lines. For example, Hassan modeled the flow field around a fish when the latter passes by or approaches an obstacle [29], moves in open water or approaches a plane surface [30], glides alongside or above a plane surface [31], and is near an oscillating sphere (also known as dipole) [32]. Ren and Mohseni derived the flow inside a trunk canal in the presence of vortex street, and examined its implications in vortex sensing [52]. Sichert *et al* explored the use of hydrodynamic multipole expansion to explain how aquatic animals distinguish shapes of moving objects [57], and in another work Sichert and van Hemmen investigated the shape influence of a submerged moving object on the lateral line perception using the conformal mapping theory [58]. Bouffanais *et al* performed analytical and numerical studies on the pressure field around a cylindrical object in a uniform flow and examined the estimation of location, size, and cross-section shape of the object based on the measured pressure field [9]. There has also been experimental work in exploring the strategies for vortex sensing [38, 5, 59] and object tracking and recognition [24].

Barring some of the aforementioned research in vortex sensing and object imaging, much of the work in information processing for biological and artificial lateral lines has been focused on dipole source localization. The dipole source emulates the rhythmic movement of fins and body appendages, and has been widely used as a stimulus (playing the role of predator, prey, or conspecific) in the study of biological lateral lines [14, 15, 19, 28]. Dipole source localization has also become a benchmark problem in the development of artificial lateral lines, for demonstration of the latter's capability in mimicking their biological counterpart. In addition, for underwater applications, localization of dipole sources has implications in detecting and estimating nearby fish-like robots and therefore is relevant to robot coordination and control.

Dagamseh *et al* proposed the use of characteristic points (zero-crossings, maxima, etc.) in the measured velocity profile along the lateral line for dipole source localization [20], similar to what was proposed by Franosch *et al* for modeling the localization by the clawed frog *Xenopus* [25]. However, this approach would require prohibitively many sensors to determine the characteristic points, and it is limited to a maximum detection distance of $1/\sqrt{2}$ body length (BL). Franosch *et al* also suggested a maximum-likelihood estimator-type model for dipole localization by *Xenopus* [25], although no algorithms were presented to solve for the optimal source location. Data-matching/table-lookup approaches were presented by Pandya *et al*, where the measured signal pattern was compared with a large, pre-obtained set of templates or an empirical model fitted with sufficient amount of data [48]. These approaches suffered from the need for excessive computing and storage resources, or the difficulty in system-level implementation [48]. Recently, a beamforming (BF) algorithm for array signal processing was used to localize a dipole source and a tail-flicking crayfish, and showed better performance than the matched filter [65]. In our prior work, we proposed a neural network-based scheme for dipole localization [3]; however, due to its black-box nature, the approach would require massive training data unless the dipole's vibration amplitude and orientation are known.

In this paper, using the analytical model for a dipole-generated flow field, we formulate a nonlinear estimation problem and present two novel iterative schemes for simultaneously localizing a dipole source and estimating its vibration amplitude and orientation. The first scheme, which is based on the Gauss–Newton (GN) method, solves the nonlinear estimation problem through iterative linearization. In the second scheme, the Newton–Raphson (NR) method is used to solve the nonlinear equation resulting from the first-order optimality condition. The flow model, with measurement noise properly incorporated, is also used to derive the Cramer–Rao bound (CRB). Analysis based on the CRB is subsequently exploited for the optimal design of intra-sensor spacing of the lateral line. Simulation is conducted to localize a dipole source placed at different points along an ellipsoidal track, with its vibration amplitude and orientation varying from one point to the next. Simulation results have shown that both the GN and NR algorithms are able to simultaneously estimate the source location, vibration amplitude and orientation with comparable precision. Furthermore, the comparison with the CRB shows that the algorithms achieve near-optimal performance at many points.

We have further validated the algorithms using an experimental prototype of lateral line that comprises six millimeter-scale IPMC flow sensors. With excellent agreement with the simulation results, the experimental results confirm that the GN and NR schemes have comparable performance in accuracy and computational efficiency with the GN scheme having a slight advantage. Specifically, for a BL of 10 cm, the maximum localization error is less than 5% of the BL when the source is within the distance of one BL. Experimental results have also shown that the proposed schemes are superior to the BF method; when the BF method is only required to determine the dipole location (with vibration amplitude/orientation given), its maximum (average, resp.)

localization error is three (four, resp.) times of those under the GN and NR schemes while consuming comparable computing time.

A preliminary version of some of the results reported in this paper was presented at the 15th International Conference on Advanced Robotics [1]. Important enhancements of this paper over [1] include CRB-based design and performance analysis for artificial lateral lines, analysis of computational complexity and storage requirement for each algorithm, more in-depth simulation analysis, experimental evaluation of the proposed recursive estimation schemes, and the inclusion of the BF method for performance comparison.

The remainder of this paper is organized as follows. The problem setup is described in section 2. The GN, NR, and BF algorithms are described in section 3, along with the CRB analysis. Simulation and experimental results are presented in sections 4 and 5, respectively. Finally, concluding remarks are provided in section 6.

2. Problem formulation

As widely assumed in the literature [28, 32, 35], we consider a potential flow generated by a vibrating sphere, the dipole source. The velocity potential φ at a spatial point can be expressed as [40]

$$\varphi(\mathbf{r}) = \frac{a^3(\mathbf{v}_\mathrm{d}\cdot\mathbf{r})}{2\|\mathbf{r}\|^3}, \tag{1}$$

where a is the diameter of vibrating sphere, $\mathbf{v}_\mathrm{d}$ is the instantaneous velocity of the dipole source, $\mathbf{r}$ represents the relative location of the point of interest with respect to the dipole, and $\|\cdot\|$ denotes the Euclidean norm of a vector. At the point $\mathbf{r}$, the flow velocity $\mathbf{v}(\mathbf{r})$ is

$$\mathbf{v}(\mathbf{r}) = -\nabla\varphi(\mathbf{r}) = \frac{a^3(3(\mathbf{v}_\mathrm{d}\cdot\mathbf{r})\mathbf{r} - \|\mathbf{r}\|^2\mathbf{v}_\mathrm{d})}{2\|\mathbf{r}\|^5}. \tag{2}$$

Since our goal in this paper is to localize the dipole source, we redefine $\mathbf{r}$ hereafter as the location of the dipole source with respect to a known point. Note that the formula (2) for the dipole-generated velocity field remains valid under the new definition of $\mathbf{r}$, because $\mathbf{v}(-\mathbf{r}) = \mathbf{v}(\mathbf{r})$. The use of the model (2) is supported by our earlier experimental work reported in [4].

To ease the discussion, we will focus on the case where the lateral line sensor and the dipole source are located in the same plane (denoted as the $x-y$ plane) in which the axis of dipole oscillation lies; see figure 1 for illustration. This is a scenario widely adopted in the study of biological and artificial lateral lines, and our proposed estimation method will extend to the more general, three-dimensional case in a straightforward manner. As depicted in figure 1, the dipole source is located at $(x_\mathrm{s}, y_\mathrm{s})$ and vibrates with velocity v^d, where the angle between the vibration axis and the x-axis is ϕ. Let an array of N sensors be located in parallel to the x-axis, with their locations assumed to be known and denoted as (x_i, y_i), $0 \leqslant i \leqslant N-1$. We assume that the presence of sensors has negligible effect on the flow distribution as characterized in (2); further discussion on sensor-flow interactions will be provided in subsection 5.2. We assume that each sensor is able to provide a noisy measurement of the local flow velocity v

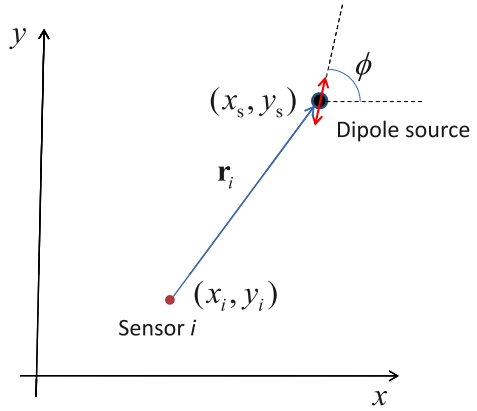

Figure 1. Illustration of the problem setup. The dipole source is located at $(x_\mathrm{s}, y_\mathrm{s})$.

along one direction, which, without loss of generality, is taken to be the x-direction in this paper. The latter consideration is motivated by the fact that most beam-like flow sensors [2, 21, 23, 43, 51, 53, 61, 64] can only sense one component of the flow velocity. In the absence of noise, from (2), we get

$$v(x_i, y_i) = \frac{a^3 v^\mathrm{d}}{2\|\mathbf{r}_i\|^5}((2(x_i - x_\mathrm{s})^2 - (y_i - y_\mathrm{s})^2)\cos\phi + 3(x_i - x_\mathrm{s})(y_i - y_\mathrm{s})\sin\phi), \tag{3}$$

where $\mathbf{r}_i = (x_i - x_\mathrm{s}, y_i - y_\mathrm{s})^T$, with '$T$' denoting the transpose.

Let the sphere vibrate with angular frequency ω and amplitude A, i.e.,

$$v^\mathrm{d} = A\sin(\omega t).$$

Furthermore, due to the periodic nature of the dipole-generated flow, we consider extracting the signal amplitude at frequency ω from each sensor as the *measurement*. In particular, given the raw signals from time n_1 to n_2, $\{s_i(n)\}_{n=n_1}^{n_2}$, the signal amplitude at ω can be readily obtained through techniques such as fast Fourier transform (FFT) [46] or sliding discrete Fourier transform (SDFT) [34, 56], and this inherent filtering process greatly reduces the noise contained in the raw sensor signal. For sensor i, the measurement M_i can then be written as

$$M_i = \left| \frac{a^3((2(x_i - x_\mathrm{s})^2 - (y_i - y_\mathrm{s})^2)\alpha_1 + 3(x_i - x_s)(y_i - y_s)\alpha_2)}{2\|\mathbf{r}_i\|^5} + d_i \right|, \tag{4}$$

where $\alpha_1 = A\cos\phi$, $\alpha_2 = A\sin\phi$, and d_i is the (amplitude) measurement noise for sensor i. Note that, to accommodate the nonnegativity constraint for the extracted amplitude, we have placed the noise d_i inside $|\cdot|$, since in general the noise could be positive or negative. The noises $\{d_i\}_{i=0}^{N-1}$ are assumed to have zero mean and be uncorrelated with each other.

Based on the sensor measurements, we are interested in estimating the location $(x_\mathrm{s}, y_\mathrm{s})$, vibration amplitude A,

and vibration direction ϕ of the dipole source. For ease of presentation, for $i = 0, \ldots, N-1$, define

$$f_i(\theta) = \frac{a^3}{2\|\mathbf{r}_i\|^5}((2(x_i - x_s)^2 - (y_i - y_s)^2)\alpha_1 + 3(x_i - x_s)(y_i - y_s)\alpha_2) \quad (5)$$

where $\theta = (\alpha_1, \alpha_2, x_s, y_s)$ represents the set of parameters to be estimated. Once θ is obtained, we can find the vibration amplitude $A = \sqrt{\alpha_1^2 + \alpha_2^2}$ and vibration orientation $\phi = \arctan(\alpha_2/\alpha_1)$. We further define

$$M \triangleq (M_0, \ldots, M_{N-1})^T,$$
$$f(\theta) \triangleq (f_0(\theta), \ldots, f_{N-1}(\theta))^T,$$
$$d \triangleq (d_0, \ldots, d_{N-1})^T.$$

We then have

$$M = |f(\theta) + d|, \quad (6)$$

where $|\cdot|$ denotes the component-wise absolute value of the vector. The estimation problem is formulated as follows. Let the dipole diameter a, frequency ω, and the sensor locations $\{(x_i, y_i)\}_{i=0}^{N-1}$ be known. Given the sensor measurement M, provide an estimate $\hat{\theta}$ for the parameter θ, such that

$$J(\hat{\theta}) = (M - |f(\hat{\theta})|)^T (M - |f(\hat{\theta})|) \quad (7)$$

is minimized, where $|f(\hat{\theta})|$ is the predicted measurement based on the estimated parameters.

Before presenting the estimation algorithms, we briefly comment on the assumptions made on the knowledge of a, ω, and $\{(x_i, y_i)\}_{i=0}^{N-1}$. Clearly, it is natural to assume knowing $\{(x_i, y_i)\}_{i=0}^{N-1}$. If the frequency ω is not given *a priori*, it can be identified through FFT of the sensor signals. Finally, if a is unknown, one will be able to estimate a^3A as a lump parameter, since that is how a and A collectively affect the flow field.

3. Estimation algorithms

In this paper we propose and compare two recursive algorithms for obtaining the parameter estimate $\hat{\theta}$ that minimizes the cost function J in (7). The function $f(\theta)$ is linear in α_1 and α_2, but highly nonlinear in (x_s, y_s). In the first algorithm, briefly summarized in subsection 3.1, $|f(\theta)|$ is linearized at each intermediate parameter estimate, and the estimate at the next iteration is obtained by solving a standard least-squares problem. This algorithm is also known as the GN method [36]. In the second algorithm, described in subsection 3.2, we first derive the (nonlinear) equation capturing the first-order necessary condition for minimizing J, and then solve the equation using the NR method [36].

We will further compare our proposed algorithms experimentally with the BF algorithm, which was one of the most competitive algorithms reported for dipole localization [65]. The algorithm will be briefly reviewed in subsection 3.3.

The CRB [18] establishes the lower limit for the variance of any unbiased estimator, and we have conducted CRB analysis for both the optimal design of a lateral line sensor and the evaluation of the proposed algorithms. The CRB analysis is presented in subsection 3.4.

3.1. GN algorithm

Linearizing the function $|f(\hat{\theta})|$ about some nominal point $\bar{\theta}$, we have

$$|f(\hat{\theta})| \approx f_L(\hat{\theta}) \triangleq |f(\bar{\theta})| + B(\bar{\theta})(\hat{\theta} - \bar{\theta}), \quad (8)$$

where

$$B(\bar{\theta}) = \left.\frac{\partial |f(\theta)|}{\partial \theta}\right|_{\theta=\bar{\theta}}.$$

The estimation problem is then converted to finding $\hat{\theta}$, such that

$$J_1(\hat{\theta}) = (M - f_L(\hat{\theta}))^T (M - f_L(\hat{\theta}))$$

is minimized. This becomes a standard least squares estimation problem, the solution of which is

$$\hat{\theta} = \bar{\theta} + \lambda(B(\bar{\theta})^T B(\bar{\theta}))^{-1} B^T(\bar{\theta})(M - |f(\bar{\theta})|), \quad (9)$$

where λ is a stepping parameter. To minimize the impact of error introduced by the linearization, a recursive version of (9) is used, where $\bar{\theta}$ is replaced by the estimate at the previous iteration:

$$\hat{\theta}_{k+1} = \hat{\theta}_k + \lambda(B(\hat{\theta}_k)^T B(\hat{\theta}_k))^{-1} B^T(\hat{\theta}_k)(M - |f(\hat{\theta}_k)|), \quad (10)$$

with $\hat{\theta}_1 = \theta_0$, an initial guess for the parameters. The algorithm is stopped when $\|\hat{\theta}_{k+1} - \hat{\theta}_k\| \leqslant \epsilon$ or $k = k_{\max}$, where $\epsilon > 0$ is a specified tolerance and $k_{\max}$ is the maximum number of allowed iterations.

We can readily estimate the computational and memory complexity of the algorithm (10). Let n_θ denote the dimension of the parameter vector θ; in the context of this paper, $n_\theta = 4$. Let $\mathcal{O}$ denote the order of magnitude. Then the following computational complexity is incurred during each iteration:

- Evaluation of $B(\hat{\theta}_k)$: $\mathcal{O}(n_\theta N)$,
- Evaluation of the product $B(\hat{\theta}_k)^T B(\hat{\theta}_k)$: $\mathcal{O}(n_\theta^2 N)$,
- Evaluation of the $n_\theta \times n_\theta$ matrix $B(\hat{\theta}_k)^T B(\hat{\theta}_k)$: $\mathcal{O}(n_\theta^3)$,
- Evaluation of the next multiplication by $B^T(\hat{\theta}_k)$: $\mathcal{O}(n_\theta^2 N)$,
- Evaluation of the final multiplication by $M - |f(\hat{\theta}_k)|$: $\mathcal{O}(n_\theta N)$,

The total computational complexity during each iteration is then $\mathcal{O}(n_\theta^3 + 2n_\theta(1 + n_\theta)N)$.

Similarly, we can evaluate the memory storage requirement:

- Storage of $\hat{\theta}_k$ and $\hat{\theta}_{k+1}$: $\mathcal{O}(2n_\theta)$,
- Storage of $B(\hat{\theta}_k)$: $\mathcal{O}(n_\theta N)$,
- Storage of the $n_\theta \times n_\theta$ matrix $B(\hat{\theta}_k)^T B(\hat{\theta}_k)$ and its inverse: $\mathcal{O}(2n_\theta^2)$,
- Storage of M and $|f(\hat{\theta}_k)|$: $\mathcal{O}(2N)$.

The total memory storage is thus $\mathcal{O}(2n_\theta + 2n_\theta^2 + (2 + n_\theta)N)$.

The computational complexity and the memory storage requirement for the GN algorithm are thus both linear in the number of sensors, N, which provides nice scalability when one is interested in a large array of sensors. With $n_\theta = 4$ and a modest sensor number N (say, $N < 20$), the algorithm is suitable for real-time execution on medium-to-high-end microcontrollers or digital signal processors that are typically used for underwater robots.

3.2. NR algorithm

The necessary condition for minimizing (7) is

$$\frac{\partial J}{\partial \hat{\theta}} = 0, \tag{11}$$

which implies

$$g(\hat{\theta}) \triangleq \left(\frac{\partial |f|}{\partial \hat{\theta}}\right)^T (M - |f(\hat{\theta})|) = 0. \tag{12}$$

An estimate of the parameter θ can then be obtained by solving the nonlinear equation (12) using the NR method:

$$\hat{\theta}_{k+1} = \hat{\theta}_k - \lambda G^{-1}(\hat{\theta}_k) g(\hat{\theta}_k), \tag{13}$$

where λ is stepping parameter, and $G(\hat{\theta})$ denotes $\frac{\partial g}{\partial \hat{\theta}}$ and can be evaluated as

$$G(\hat{\theta}) = \sum_{i=0}^{N-1} (M_i - |f_i(\hat{\theta})|) \frac{\partial^2 |f_i|}{\partial \hat{\theta}^2} - \left(\frac{\partial |f_i|}{\partial \hat{\theta}}\right)^T \left(\frac{\partial |f_i|}{\partial \hat{\theta}}\right).$$

The starting value $\hat{\theta}_1$ in (13) is set to be θ_0, an initial guess of the parameters. Similar to the GN method, the iteration in (13) is stopped when $\|\hat{\theta}_{k+1} - \hat{\theta}_k\| \leqslant \epsilon$ or $k = k_{\max}$ for prespecified ϵ and $k_{\max}$.

Following similar analysis as in section 3.1, we can show that the computational complexity and memory storage requirement for each iteration of the NR algorithm are $\mathcal{O}(n_\theta^2 + n_\theta^3 + n_\theta(1 + 2n_\theta)N)$ and $\mathcal{O}(3n_\theta + 2n_\theta^2 + (2 + n_\theta + n_\theta^2)N)$, respectively. They again show linear scalability with N, indicating the promise of the algorithm in real-time applications.

3.3. BF algorithm

The BF algorithm based on Capon's method was used by Yang *et al* to estimate a five-dimensional (5D) dipole state (3D location and 2D vibration orientation) [65]. In our dipole localization setup, the dipole state is fully captured by the 4D parameter vector θ. Given the raw sensor signals for instantaneous flow velocities (projected into the sensing axes), denoted as $\{s_0(n), \ldots, s_{N-1}(n)\}_{n=n_1}^{n_2}$, one constructs an energy-like map $E(\hat{\theta})$, which indicates how likely the actual dipole state is $\hat{\theta}$. The optimal estimate of θ is then obtained as

$$\hat{\theta}^* = \arg\max_{\hat{\theta}} E(\hat{\theta}). \tag{14}$$

In order to evaluate $E(\hat{\theta})$, one first evaluates the correlation matrix R based on the measurements from all sensors:

$$R = \frac{1}{n_2 - n_1} \sum_{n=n_1}^{n_2} S(n) S^T(n),$$

where $S(n) = [s_0(n), \ s_1(n), \ldots, s_{N-1}(n)]^T$. The energy-like function E is then computed as

$$E(\hat{\theta}) = \frac{1}{|f(\hat{\theta})|^T R^{-1} |f(\hat{\theta})|}. \tag{15}$$

To search for the maximizing $\hat{\theta}$ for E, one typically scans through the space for the dipole state [65]. The latter involves creating a discrete grid of dipole state components, and the resulting total number of grid points increases exponentially with the dimension of the dipole state.

Let $n_s = n_2 - n_1$, and let n_g denote the number of the grid points for the parameter space. Then it can be shown that the computational complexity of the BF algorithm is $\mathcal{O}((n_s + 2n_g)N^2 + N^3)$, and the memory storage requirement is $\mathcal{O}(n_g + n_s N + 2N^2)$. The numbers n_s and n_g are typically very large; for example, even if one discretizes each parameter into only ten levels, n_g would be 10^4. In addition, the N^3 dependence on the sensor number shows that the algorithm is computationally demanding when the number of sensors is relatively large.

3.4. CRB analysis

Consider (4). For the CRB analysis, we assume that the noise d_i from each sensor is Gaussian with zero mean and variance σ^2. Given the dipole state θ, the probability for the sensors to have the measurement $M = (M_0, \ldots, M_{N-1})^T$ is expressed as

$$P(M, \theta) = \prod_{i=0}^{N-1} \frac{1}{(2\pi\sigma^2)^{1/2}} (\mathrm{e}^{\frac{-1}{2\sigma^2}(M_i - f_i(\theta))^2} + \mathrm{e}^{\frac{-1}{2\sigma^2}(-M_i - f_i(\theta))^2}), \tag{16}$$

$$= \prod_{i=0}^{N-1} \frac{2}{(2\pi\sigma^2)^{1/2}} \left(\mathrm{e}^{\frac{-M_i^2}{2\sigma^2}} \mathrm{e}^{\frac{-f_i^2(\theta)}{2\sigma^2}} \cosh \frac{M_i f_i(\theta)}{\sigma^2}\right). \tag{17}$$

The log-likelihood function is then

$$\ln P(M, \theta) = N \frac{2}{(2\pi\sigma^2)^{1/2}} - \frac{1}{2\sigma^2} \sum_{i=0}^{N-1} M_i^2 - \frac{1}{2\sigma^2} \sum_{i=0}^{N-1} f_i^2(\theta) + \sum_{i=0}^{N-1} \ln \left(\cosh \frac{M_i f_i(\theta)}{\sigma^2}\right). \tag{18}$$

The Fisher information matrix $I(\theta)$ can then be derived as

$$\begin{aligned} I(\theta) &= -\mathbf{E}\left[\frac{\partial^2 \ln P(M; \theta)}{\partial \theta^2}\right] \\ &= \frac{1}{\sigma^2} \sum_{i=0}^{N-1} \left\{ f_i(\theta) \frac{\partial^2 f_i(\theta)}{\partial \theta^2} + \left[\frac{\partial f_i(\theta)}{\partial \theta}\right]\left[\frac{\partial f_i(\theta)}{\partial \theta}\right]^T \right. \\ &\quad \left. - \int_{M_i=0}^{\infty} g_i(M_i, \theta) P_i(M_i, \theta) \mathrm{d}M_i \right\}, \end{aligned} \tag{19}$$

where $\mathbf{E}[\cdot]$ denotes the expectation,

$$\begin{aligned} g_i(M_i, \theta) &\triangleq \tanh\left(\frac{M_i f_i(\theta)}{\sigma^2}\right) M_i \frac{\partial^2 f_i(\theta)}{\partial \theta^2} \\ &\quad + \frac{M_i^2}{\sigma^2}\left[\frac{\partial f_i(\theta)}{\partial \theta}\right]\left[\frac{\partial f_i(\theta)}{\partial \theta}\right]^T \left[1 - \tanh^2 \frac{M_i f_i(\theta)}{\sigma^2}\right], \end{aligned} \tag{20}$$

$$P_i(M_i, \theta) = \frac{1}{(2\pi\sigma^2)^{1/2}} \{\mathrm{e}^{\frac{-1}{2\sigma^2}(M_i - f_i(\theta))^2} + \mathrm{e}^{\frac{-1}{2\sigma^2}(-M_i - f_i(\theta))^2}\}. \tag{21}$$

The appendix provides the intermediate steps for arriving at (19). Note that $I^{-1}(\theta)$ represents the lower bound (CRB) on the estimation variance for any unbiased estimator of θ;

specifically, the variance of the jth component of $\hat{\theta}$, denoted as $\hat{\theta}_{[j]}$, satisfies

$$\mathrm{Var}(\hat{\theta}_{[j]}) \geqslant [I^{-1}(\theta)]_{j,j}, \quad j = 1, \ldots, 4. \tag{22}$$

In section 4, we will illustrate the use of (22) for the optimal design of a lateral line sensor and for the localization performance evaluation of the proposed estimation algorithms.

4. Simulation results

4.1. CRB-based optimal design of lateral line sensor

The CRB analysis presented in subsection 3.4 can be used for the optimal design of a lateral line system, including both the number of flow sensors and the geometric arrangement of these sensors. The latter point is illustrated here with an example of optimizing the intra-sensor spacing, which is later adopted in the construction of an experimental prototype. We consider a working area of 20×10 cm^2 ($-10 \leqslant x \leqslant 10$, $0 < y \leqslant 10$), and assume that the lateral line consists of six flow sensors, uniformly distributed along the x-axis and centered at the origin. We would like to determine the sensor-to-sensor spacing that minimizes the localization error, in a sense that will be described next.

Additional parameters for the optimization problem, largely motivated by our experimental setup, include sphere diameter $a = 1.9$ cm, vibration frequency 40 Hz, and vibration amplitude $A = 0.191$ cm. Note that the choice of different values for a, A, and vibration frequency will not have impact on the optimal design since it will simultaneously scale the sensor outputs by the same amount. In order to ensure good localization performance when the dipole is at different locations and vibrating with different orientations within the working area, we divide the area into a grid of 1×1 cm^2 cells, resulting in a total of 210 grid points ($x = 0, \pm 1, \ldots, \pm 10$, $y = 1, 2, \ldots, 10$). And at each grid point, we consider 12 orientations $\phi(n) = \pi/n$, $n = 1, 2, \ldots, 12$, that uniformly span the orientation space.

For a given intra-sensor spacing, for each grid point $(x(k), y(k))$, $1 \leqslant k \leqslant 210$, and each orientation $\phi(n)$, $1 \leqslant n \leqslant 12$, we evaluate the corresponding CRBs, $C_x(k, n)$, $C_y(k, n)$, $C_{\alpha_1}(k, n)$, and $C_{\alpha_2}(k, n)$ for the estimation variances $\sigma_x^2(k, n)$, $\sigma_y^2(k, n)$, $\sigma_{\alpha_1}^2(k, n)$, and $\sigma_{\alpha_2}^2(k, n)$, respectively. Due to the different meanings and units for $C_x(k, n)$, $C_y(k, n)$, $C_{\alpha_1}(k, n)$, and $C_{\alpha_2}(k, n)$, we introduce a normalization scheme for these CRB elements so that they can be properly combined into a single quantity for optimization: for $p = x, y, \alpha_1, \alpha_2$, define

$$\mu_p(k) = \max_{n=1,2,\ldots,12} C_p(k, n). \tag{23}$$

The cumulative uncertainty for a given intra-sensor spacing is then obtained as

$$U_c = \frac{1}{12} \sum_{k=1}^{210} \sum_{n=1}^{12} \left(\frac{C_x(k, n)}{\mu_x(k)} + \frac{C_y(k, n)}{\mu_y(k)} + \frac{C_{\alpha_1}(k, n)}{\mu_{\alpha_1}(k)} + \frac{C_{\alpha_2}(k, n)}{\mu_{\alpha_2}(k)} \right).$$

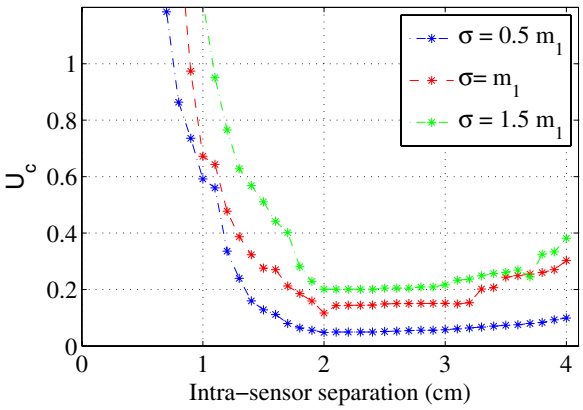

Figure 2. CRB-based cumulative uncertainty in localization as a function of intra-sensor spacing.

Figure 2 shows the cumulative uncertainty U_c as a function of the intra-sensor spacing, for three different noise variances σ^2 for the measurement noise. Here $m_1 = 0.0065$ cm^2 s^{-2} represents a typical value of variance for our IPMC prototype flow sensors. It is clear that there is an optimal range (around 2 cm) for the intra-sensor distance where the cumulative localization uncertainty is minimized. Larger or smaller spacing leads to bigger uncertainty. This can be explained as follows. When the sensors are too packed, they cannot pick up sufficiently distinct signals (think about the extreme case of all sensors stacked together) and cannot cover a wide area with large signal-to-noise ratio (SNR). On the other hand, when the sensors are very far apart, some sensors become too distant from the dipole source and their SNRs become very low, negatively impacting the localization performance. Another interesting observation from figure 2 is that, the optimal intra-sensor spacing is not sensitive to the value of the noise variance. This is a positive news for the design, since it is often difficult to know the precise value of σ^2 in practice.

4.2. Localization of dipole source with unknown vibration amplitude and orientation

We now present simulation results on the performance of the proposed GN and NR schemes on localizing a dipole source with unknown vibration amplitude and orientation. Figure 3 illustrates the simulation setup. The lateral line system, consisting of six flow sensors with intra-sensor spacing of 2 cm, is placed parallel to the x-axis and centered at the origin. The dipole source is placed at 19 different locations along an ellipsoidal track that is centered at $(0, 6)$ cm. Specifically, the dipole locations are prescribed by

$$(x_s(k), y_s(k)) = (10 \cos \psi(k), 6 + 4 \sin \psi(k)), \quad k = 1, 2, \ldots, 19, \tag{24}$$

where $\psi(k) = \frac{(k-1)\pi}{9}$. Note that point 1 and point 19 overlap, as shown in figure 3. The sphere diameter a, vibration frequency, and the measurement noise variance σ^2 are set to be 1.9 cm, 40 Hz, and m_1 (0.0065 cm^2 s^{-2}), respectively.

4.2.1. The role of sensor array in resolving location ambiguity. Before presenting the simulation results on localization, we

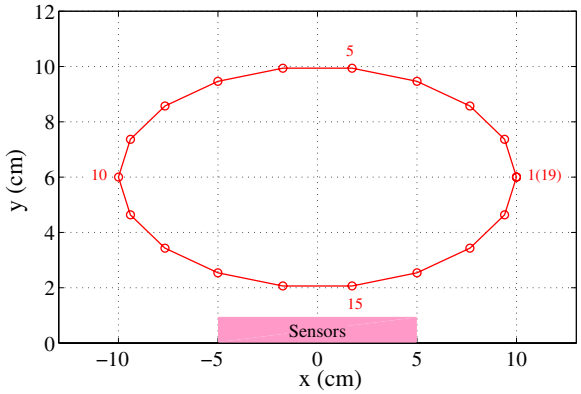

Figure 3. Illustration of the simulation setup, where 19 points as indexed in the figure will be localized.

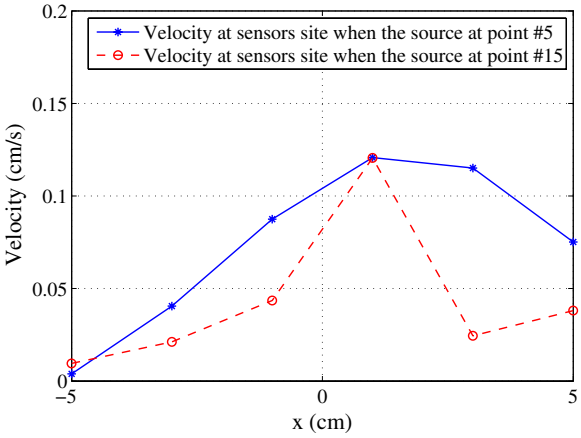

Figure 4. Illustration of the capability of a sensor array to resolve the ambiguity in source locations. A source at point 5 and point 15 produces the same output for sensor 4 when vibrating with two different amplitudes, but the corresponding outputs for other sensors are distinct for the two source locations.

illustrate the advantage of a flow sensor array in resolving the challenge of localization ambiguity faced by a single sensor, where a closer source with smaller-amplitude vibration could produce the same output as a farther source with larger-amplitude vibration. Figure 4 shows the flow velocities at the six sensor sites when the source is at two different locations, point 5 and point 15 as illustrated in figure 3. At point 5, the source is assumed to vibrate with an amplitude of 0.141 cm and an orientation of 0°, and at point 15 (which is closer to the sensors), the source is assumed to vibrate with the same orientation but an amplitude of 0.0022 cm. As can be seen from figure 4, while the source produces the same flow velocity (x-component) for the sensor located at $(1, 0)$ cm (the fourth sensor from the left), the flow velocities at other sensor sites are quite different under the two source locations. Such distinct profiles of sensor array output offer the opportunity to uniquely identify the location of a source.

4.2.2. Results on source localization. In order to test the algorithms' capability in estimating vibration amplitude A and orientation ϕ in addition to the source location, we vary A (in cm) and ϕ along the track as follows:

$$A(k) = 0.191 - 0.01(k-1), \tag{25}$$

$$\phi(k) = \frac{(k-1)\pi}{9}. \tag{26}$$

The stopping criterion ϵ for both the GN algorithm and the NR algorithm is chosen to be 0.01, and the maximum number of iterations is set to be $k_{\max} = 2500$. Figure 5(a) shows the actual and estimated source locations under the GN method and the NR method for a typical run. It can be seen that the localization is well accomplished under both schemes. Furthermore, figure 5(b) shows the localization error for each of the 19 points on the track, where the error is defined as the Euclidean distance between the actual and estimated locations. The two proposed methods have comparable performance in terms of the localization error. The maximum error under the GN method is 0.38 cm and that under the NR method is 0.39 cm. Figure 6(a) shows the estimated source vibration amplitudes and the estimation errors for both methods. The maximum amplitude error is 0.0013 and 0.0015 cm for the GN and NR methods, respectively. Figure 6(b) shows the estimated source vibration orientations and the corresponding errors. The maximum orientation error is 0.12 and 0.13 rad for the GN and NR methods, respectively. From figures 5 and 6, we can see that both the GN and NR methods are able to simultaneously estimate the location, vibration amplitude, and vibration orientation successfully. In addition, while the GN method has slightly higher estimation accuracy for all variables, the overall performances of the two methods are quite close.

Table 1. Average computational time per localization point for different values of convergence threshold ϵ.

ϵ	Average time under GN (s)	Average time under NR (s)
0.05	0.95	1.14
0.01	1.1	1.2
0.001	2.2	2.24

4.2.3. The impact of threshold ϵ. We have examined the impact of threshold ϵ on the estimation accuracy and computational time. The simulation described in section 4.2.2 is repeated for two additional values of ϵ, 0.05 and 0.001. Figure 7 shows the localization errors under the proposed GN and NR algorithms for different values of ϵ. It can be seen that, while there is considerable reduction of error when ϵ is reduced from 0.05 to 0.01, there is no gain in estimation accuracy when ϵ is reduced from 0.01 to 0.001. This shows that, due to the noise in the sensor measurement, there is a limit on ϵ beyond which the performance cannot be further improved. Table 1 lists the average computational time per localization point with different ϵ values. Here the computational time is based on the simulation in Matlab on a Samsung laptop with a 2.53 GHz processor and 4 GB RAM, where the localization is executed for seven times and the average of times taken for those executions is obtained. As expected, there is a monotonic

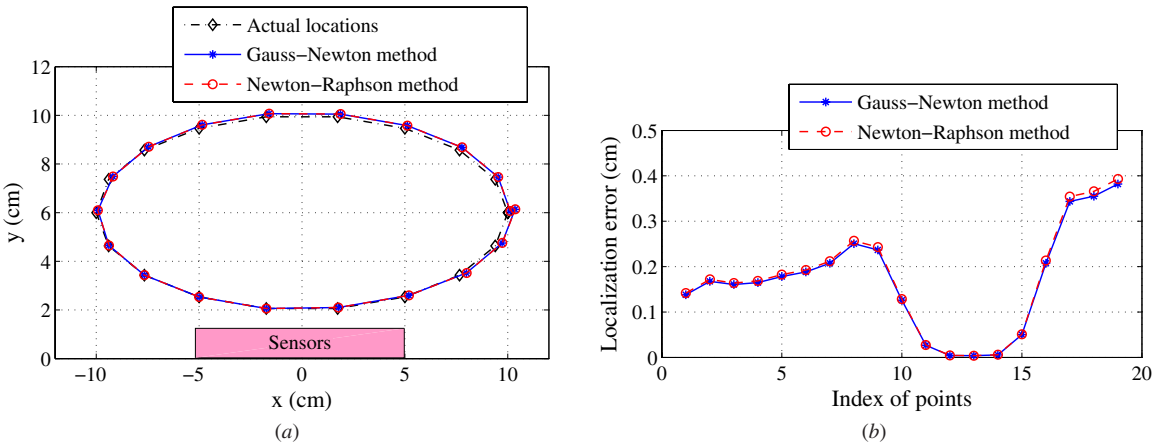

Figure 5. Simulation results. (*a*) Estimation of source locations; (*b*) localization errors at the 19 points.

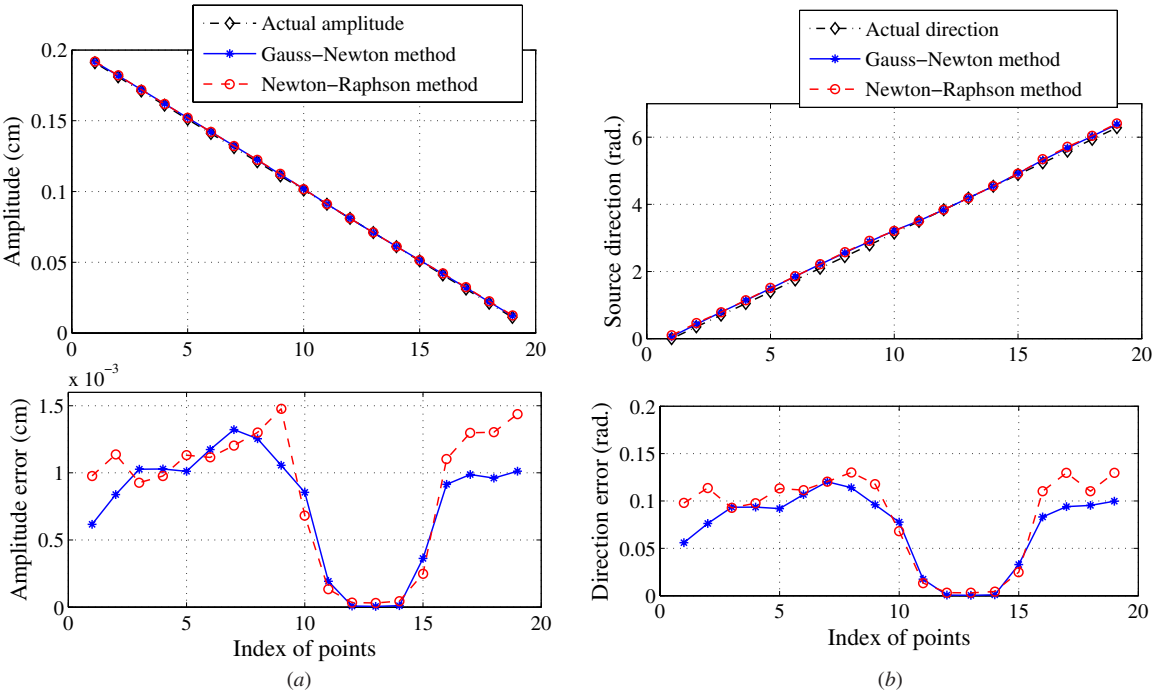

Figure 6. Simulation results. (*a*) Estimation of the source vibration amplitudes; (*b*) estimation of the source vibration orientations.

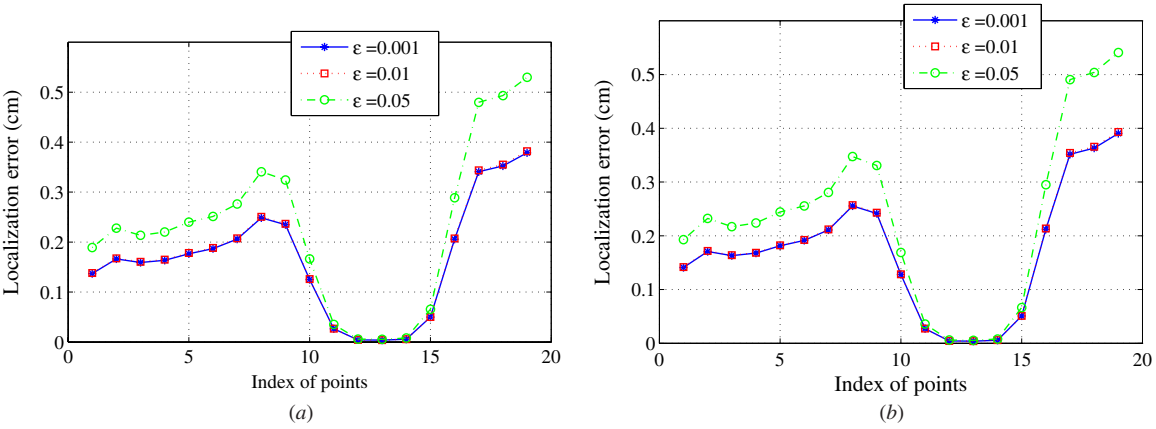

Figure 7. Simulation results: localization errors at the 19 points when different values for convergence threshold ϵ are used: (*a*) under the GN algorithm; (*b*) under the NR algorithm.

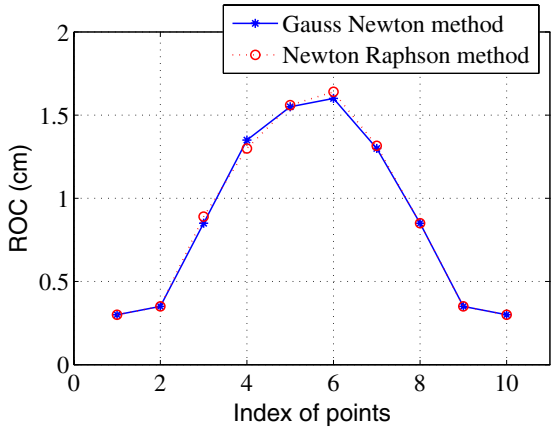

Figure 8. The radius of the ROC when the source is located at points 1–10.

relationship between the computational time and ϵ; however, this relationship is highly nonlinear. This is partly due to the fact that, for $\epsilon = 0.001$, the algorithms are mostly terminated when the iteration number k reaches $k_{\max}$. In summary, for a given problem setup, there is an optimal ϵ that results in the best estimation performance while consuming the least amount of computing time for achieving that performance. In practice, such an ϵ can be identified through simulating the algorithms with empirically characterized noise variances for the sensors.

4.2.4. The role of initial values: region of convergence. We have further investigated the impact of the initial estimate of parameters on the convergence of the algorithms. Figure 8 shows the computed radius of the region of convergence (ROC), for each of the two algorithms, at points 1–10 as illustrated in figure 3. The ROC radius at each point i represents the radius of the largest circle around point i, such that any initial location estimate within that circle will result in the convergence of the algorithm to point i. From figure 8, both the GN and NR algorithms have finite ROC radii, which are comparable to each other. In addition, the ROC seems to be the largest when all sensors have relatively high output (when the source is at point 6). It should be noted though, that the actual ROC is most likely not a disk; therefore, the estimate of ROC shown in figure 8 is conservative. Finally, while the results in figure 8 suggests the importance of properly choosing initial parameter estimates for each source location, in practice, when tracking a moving dipole, one can simply use the results for a previous location as the initial estimate for the current location, as long as a relatively accurate initial estimate is provided for the very first location.

4.3. Further CRB analysis on performance

We have further used the CRB analysis to evaluate the localization performance of our proposed methods. In this evaluation, a similar setup as in subsection 4.2 is considered, except that we fix the vibration amplitude and orientation at all points to be 0.191 cm and 0°, respectively, and treat them as known. We run the simulation of localizing the 19 points using the GN and NR algorithms for 20 times, based on which the empirical estimation variances σ_x^2 and σ_y^2 for x_s and y_s are obtained. Figure 9 shows the comparison of the square-roots of empirical variances with those of the corresponding CRBs. It is clear that the CRBs are lowest when the source location is closest to the lateral line (points 13–16), which is explained by the highest SNRs at those locations. The empirical estimation variances under both schemes are higher than the CRBs; however, the differences are not big, especially at the points where the SNRs are large. This analysis confirms that the proposed GN and NR schemes deliver close-to-optimal estimation performance.

5. Experimental results

5.1. Experimental setup

We have experimentally examined the performance of the proposed GN and NR algorithms and the BF algorithm reported in the literature, using an artificial lateral line prototype consisting of six IPMC sensors, shown in figure 10. An IPMC has three layers, with an ion-exchange polymer membrane sandwiched by metal electrodes. Inside the polymer, (negatively charged) anions covalently fixed to polymer chains are balanced by mobile, (positively charged)

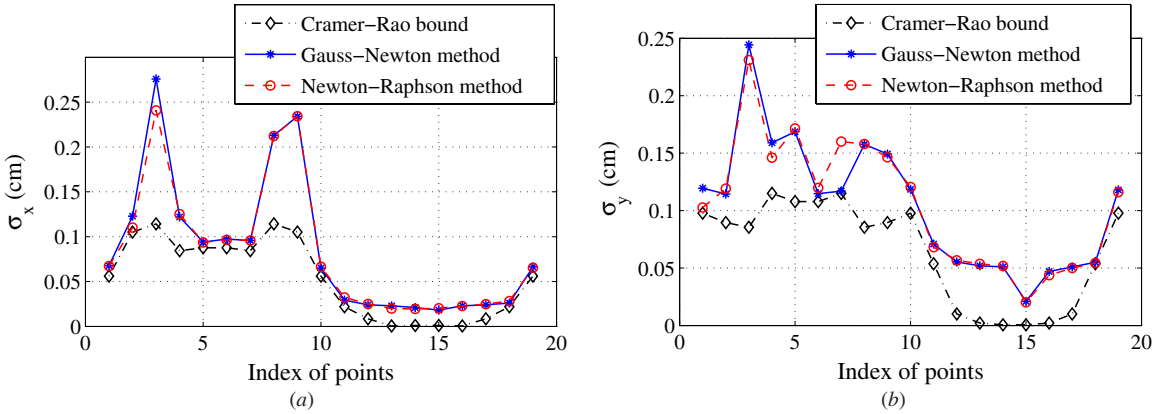

Figure 9. Simulation results: comparison of square-roots of empirical estimation variances (*a*) σ_x and (*b*) σ_y with the square-roots of corresponding CRBs.

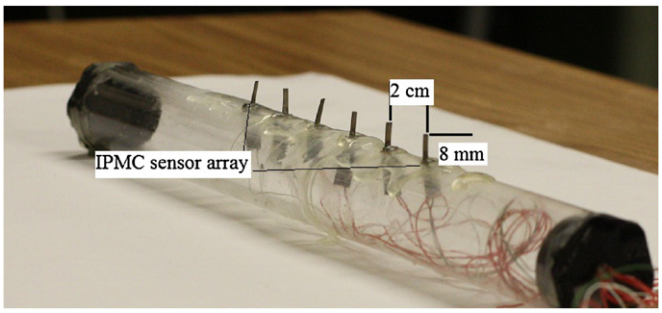

Figure 10. An experimental prototype of IPMC-based lateral line system.

cations. Deformation under a mechanical perturbation redistributes the cations, producing a detectable electric signal (e.g., short-circuit current) that is well correlated with the mechanical stimulus, which explains the sensing principle of an IPMC [55]. Each sensor in our lateral line prototype, measuring 8 mm long, 2 mm wide, and 200 μm thick, was cut from an IPMC sheet fabricated by the Smart Microsystems Laboratory at Michigan State University, following a recipe similar to the one described in [37]. Based on the optimization results from CRB analysis (subsection 3.4), the intra-sensor separation was set to be 2 cm, resulting in a total span of 10 cm for the sensor. The latter can be considered as the BL of the lateral line system. We will test the capability of the system in localizing a dipole source within a distance of about one BL, which is the typical working range for biological lateral lines. All sensors can bend in the direction that is parallel to the lateral line, thus measuring the flow component in the same direction.

Figure 11(a) illustrates the experimental setup. Experiments are conducted in a tank that is 6 feet long, 2 feet wide, and 2 feet deep. The short-circuit current output of each IPMC sensor is amplified with a two-stage amplification circuit, the details of which can be found in [26]. Acquisition and processing of the IPMC sensor output are conducted through a dSPACE system (DS1104, dSPACE Inc., Germany). A digital low-pass filter is further implemented to remove high-frequency noises from the sensor signals. The dipole source is created with a mini-shaker (Model 4810, Brüel & Kjaer, Denmark) (figure 11(b)), the vibration amplitude and frequency of which can be readily controlled through a voltage input to the mini-shaker. A lightweight bar firmly attached to the mini-shaker then translates the vibration to a sphere rigidly coupled to the bar. The sphere, which is a aluminum ball, has a diameter of 1.9 cm. The sphere and the IPMC sensors are submerged underwater, about 5 cm from the water surface. The dipole source location and vibration direction with respect to the IPMC lateral line can be adjusted by moving the stand holding the IPMC lateral line. The dipole frequency is chosen to be 40 Hz, which is in the typical range for the study of biological and artificial lateral lines. The vibration amplitude of the sphere is measured with a laser displacement sensor (OADM 20I6441/S14F, Baumer Electric).

5.2. Calibration of IPMC sensors

The relationship between the current output I of an IPMC sensor and the local flow velocity v can be captured by the cascaded connection of fluid–structure interaction dynamics G_1 and IPMC transduction dynamics G_2, both of which can be treated as linear when the flow is relatively small. The dynamics G_1 describes how the tip displacement q of the sensor beam responds to the flow v, and can be modeled following the approach presented by McHenry *et al* in modeling the interactions between a superficial neuromast and the ambient flow [44]. The dynamics G_2, on the other hand, relates the current output I to the tip displacement q and can be captured with a physics-based model [11]. It can be shown that, based on the physical parameters for the IPMC sensors and the operating frequency in our experiments, the transfer function $G_1(s)$ can

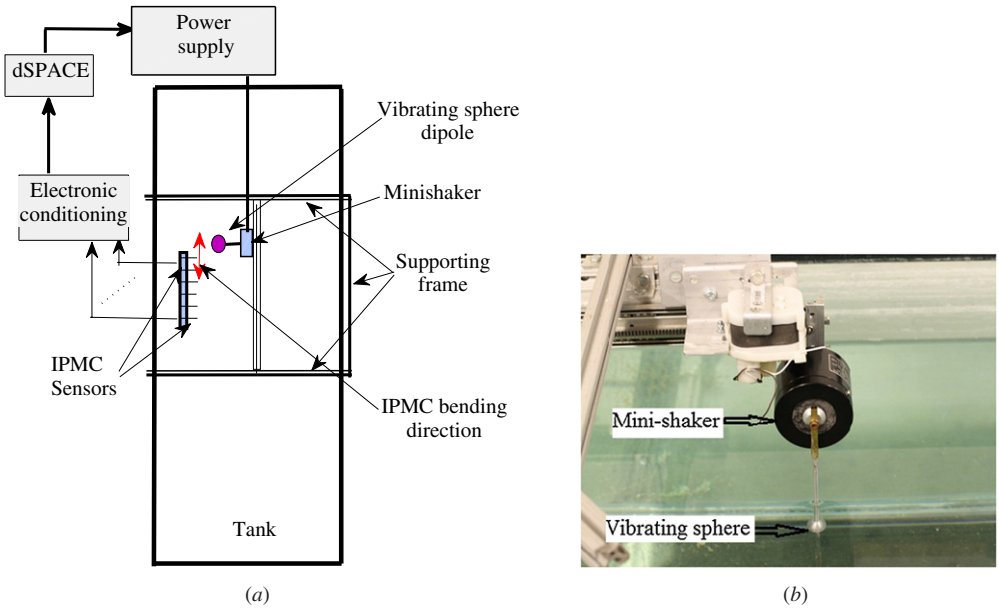

(a) (b)

Figure 11. Experimental setup. (a) Schematic of the experimental system; (b) the dipole source.

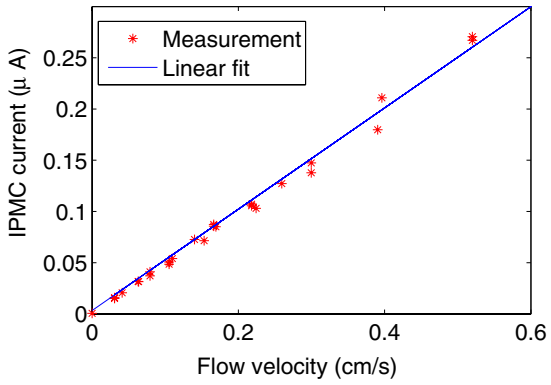

Figure 12. Illustration of IPMC sensor calibration.

be approximated by [44]

$$G_1(s) = \frac{q(s)}{v(s)} = \frac{c_1}{s}, \tag{27}$$

and G_2 by [10]

$$G_2(s) = \frac{I(s)}{q(s)} = c_2 s, \tag{28}$$

where s is the Laplace variable, and c_1 and c_2 are lumped physical constants. The detailed derivation and approximation of G_1 and G_2 are outside the scope of this paper, and hence omitted here in the interest of brevity.

From (27) and (28), the short-circuit current output of an IPMC sensor is (approximately) proportional to the instantaneous local flow velocity. The proportionality constant can vary from sensor to sensor because of the spatial inhomogeneity in the fabricated IPMC material, difference in exact sensor dimensions, and discrepancy across different channels of the sensing circuit. The constant is identified through a calibration procedure described next. We put the mini-shaker-based dipole source at different locations with respect to each sensor and extracted the amplitude of sensing current with FFT. The theoretical value of the flow velocity at the location of the sensor is obtained using (5). Figure 12 shows the IPMC signal amplitude versus the theoretical local velocity for one IPMC sensor, from which an approximately linear relationship between the sensor output I and the flow velocity v parallel to the lateral line can be observed. The proportional constant $\eta = \frac{I}{v}$ is identified using the Matlab command polyfit$(\cdot, \cdot, 1)$.

The proportionality constants identified for the six IPMC sensors are $\eta_1 = 0.49\ \mu\text{A}(\text{cm s}^{-1})^{-1}$, $\eta_2 = 0.21\mu\text{A}(\text{cm s}^{-1})^{-1}$, $\eta_3 = 0.165\ \mu\text{A}(\text{cm s}^{-1})^{-1}$, $\eta_4 = 0.23\ \mu\text{A}(\text{cm s}^{-1})^{-1}$, $\eta_5 = 0.24\ \mu\text{A}(\text{cm s}^{-1})^{-1}$, and $\eta_6 = 0.3\ \mu\text{A}(\text{cm s}^{-1})^{-1}$. Given η_i, the flow velocity at the site of sensor i is calculated from the sensor output I_i via

$$v_i = \frac{I_i}{\eta_i}.$$

5.3. Experimental results on dipole source localization

We have conducted localization experiments in a very similar setup as for the simulation (see figure 3). Specifically, we have placed the dipole source (relative to the lateral line) at 19 points along an ellipsoidal track centered at (0, 6) cm, as prescribed by (24). The vibration amplitude at each point varies according to (25). Due to the difficulty in precisely orienting the dipole vibration axis, we have chosen to use only two different orientations, 0 and $\frac{\pi}{2}$ rad. In particular, we set

$$\phi(k) = \begin{cases} 0, & k = 1, \ldots, 10 \\ \dfrac{\pi}{2}, & k = 11, \ldots, 19 \end{cases}$$

For each location, sensor outputs of 10 s are acquired at a sampling rate of 1 kHz. FFT is performed on the data to extract the signal amplitudes, which are then used for estimation with the GN and NR methods. For comparison purposes, the same (raw) sensor data have been used for estimation using the BF algorithm; see the description in subsection 3.3.

Figure 13 shows the experimental results on the localization. It is notable that the localization performance has only slightly degraded from that in simulation (figure 5). The maximum localization errors for the GN and NR methods are 0.46 and 0.48 cm, respectively, which occur at point 19, where the vibration amplitude is the smallest. Figures 14(a) and (b) show the estimated source vibration amplitudes and source vibration directions at the 19 points. For both methods, the maximum errors in the amplitude estimation are around 0.002 cm, about 50% larger than those in simulation. The maximum errors in the orientation estimation are around 0.12 rad, which are almost the same as those in simulation; this might be explained by the fact that only two different orientations were tested in the experiments. Another observation is that, in consistency with the simulation results, the GN method has demonstrated slightly better performance than the NR method.

We have further examined the performance of the BF algorithm on the same data. In order to create the energy-like map for each dipole state, one needs to discretize the space for the dipole state (location, vibration amplitude, and vibration orientation). Clearly, the resolution of the discretization has a direct impact on the estimation performance; a finer grid is expected to produce more accurate resolution (sharper map), but at the cost of computational time. To ease the computation, we have assumed that the vibration amplitude and orientation at each location are known, and thus focused on only the estimation of source location. We have used three different resolutions for discretizing the working area, $0.02 \times 0.02\ \text{cm}^2$, $0.05 \times 0.05\ \text{cm}^2$, and $0.1 \times 0.1\ \text{cm}^2$. The dipole location is estimated by visually finding the maximum of the energy-like map. As an illustration, figure 15 shows the energy-like map when the dipole source is placed at point 3, with the $0.1 \times 0.1\ \text{cm}^2$ discretization grid, where the peak is clearly visible.

Figure 16 shows the localization results corresponding to the three discretization schemes under the BF approach. As one would expect, the localization error decreases as the grid gets finer; however, the error does not scale linearly with the grid resolution. The maximum localization errors for the three discretization schemes (finer to coarser) are 0.91 cm, 1.1 cm, and 1.33 cm, respectively. For a more clear comparison, table 2 summarizes the average and maximum localization errors for

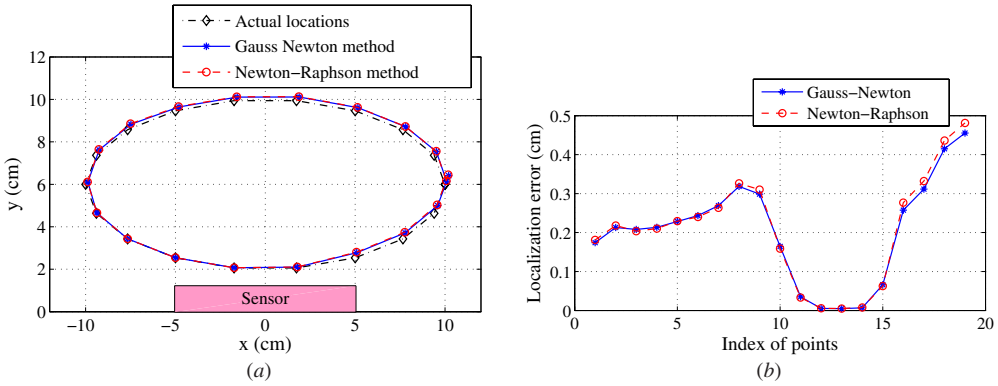

Figure 13. Experimental results: (*a*) estimation of source locations; (*b*) localization errors at the 19 points.

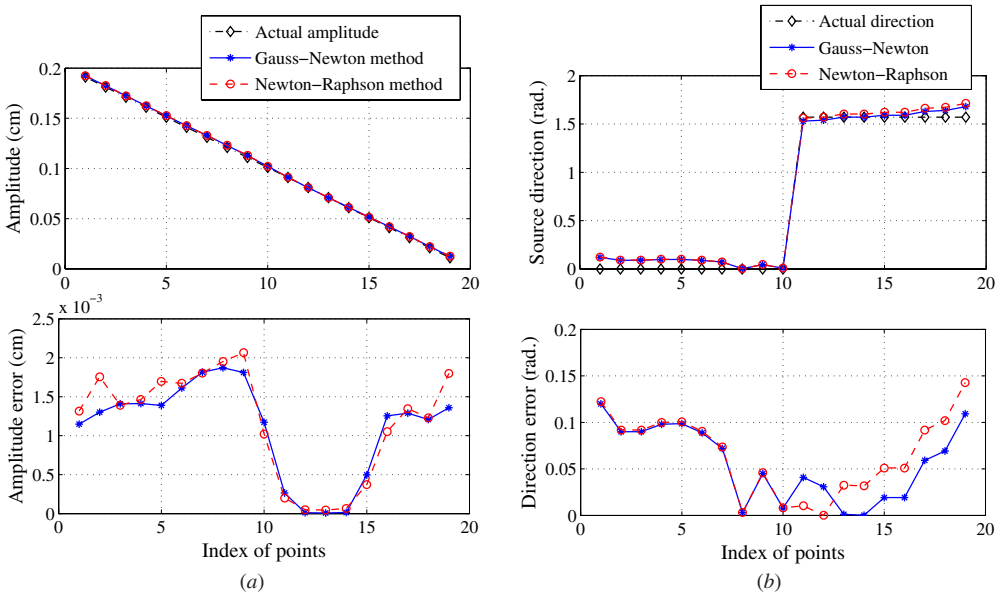

Figure 14. Experimental results: (*a*) estimation of the source vibration amplitudes; (*b*) estimation of the source vibration orientations.

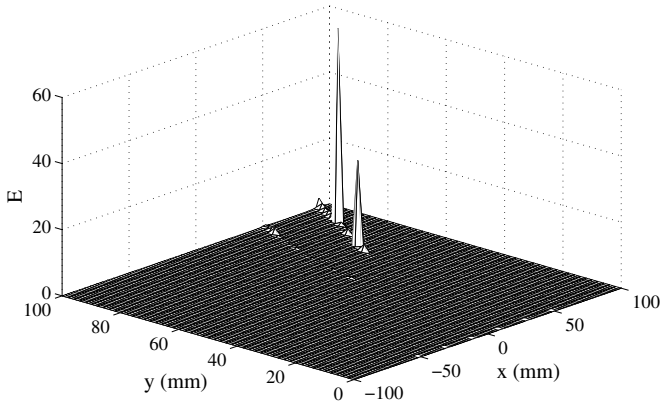

Figure 15. Experimental results: constructed energy-like map when the dipole is located at point 3 (0.1 × 0.1 cm^2 grid).

the 19 points, for the GN, NR, and three BF algorithms. It can be seen that, with the finest grid (0.02 × 0.02 cm^2), the BF algorithm results in an average/maximum localization error that is twice as much as what is resulted from the GN and NR algorithms.

Table 2. Experimental results: maximum and average estimation errors under different algorithms. 'BF (0.02)' stands for BF with 0.02 × 0.02 cm^2 grid, and similar interpretations apply for 'BF (0.05)' and 'BF (0.1)' . Note that vibration amplitude and orientation are assumed known for the BF algorithms.

Algorithms	GN	NR	BF (0.02)	BF (0.05)	BF (0.1)
Average localization error (cm)	0.21	0.21	0.48	0.65	0.89
Max. localization error (cm)	0.46	0.48	0.91	1.1	1.33
Average amplitude error (cm)	0.0014	0.0014	–	–	–
Max. amplitude error (cm)	0.0019	0.0021	–	–	–
Average orientation error (rad)	0.1	0.1	–	–	–
Max. orientation error (rad)	0.12	0.14	–	–	–

To put the comparison in perspective, we have further recorded the computation time taken by each algorithm. The localization problem at all 19 points is executed under each

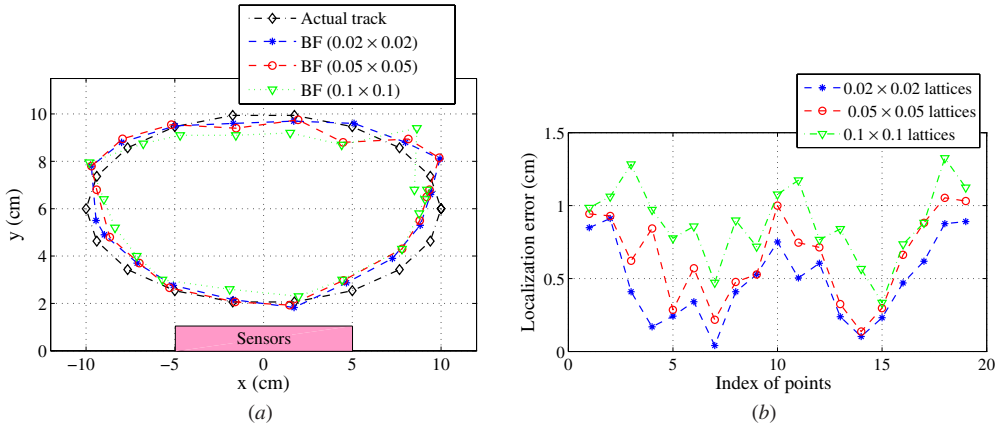

Figure 16. Experimental results: localization of the dipole source using the BF algorithm: (*a*) estimation of the source locations; (*b*) localization errors at the 19 points.

Table 3. Average computational time per localization point for different algorithms.

Algorithms	Average time (s)
GN	1.1
NR	1.2
BF (0.02 × 0.02 cm^2)	11.2
BF (0.05 × 0.05 cm^2)	2.1
BF (0.1 × 0.1 cm^2)	1.26

algorithm for seven times, and table 3 summarizes the average time per point taken by each algorithm. Note that for GN and NR, the computation includes FFT and executing the recursive update until convergence, and for the BF algorithm, the computation includes evaluating the correlation matrix and constructing the energy-like map. From table 3, it can be seen that GN is slightly more efficient than NR. With a discretization grid of 0.1 × 0.1 cm^2, the BF algorithm takes a comparable amount of computation time as GN or NR; however, from table 2, the corresponding maximum localization error is three times as much. Considering that the GN and NR algorithms simultaneously estimate four variables while the BF algorithm only does two (in this setup), we can conclude that the proposed GN and NR algorithms are more accurate and computationally efficient than the BF algorithm. One likely reason that the BF algorithm produces larger estimation error is the noise in the raw signals from IPMC sensors, which would have a lesser impact for the GN and NR schemes because of the FFT procedure.

6. Conclusion

In this paper we proposed and examined in detail two iterative schemes for dipole source localization based on measurements from an artificial lateral line. The schemes, referred to as Gauss–Newton (GN) algorithm and Newton–Raphson (NR) algorithm, respectively, were derived with a nonlinear estimation perspective to simultaneously estimate the dipole location, vibration amplitude, and vibration orientation. We performed CRB analysis based on the analytical flow model, and demonstrated its use in the design of the lateral line system via the example of optimizing intra-sensor spacing. The CRB analysis was also used later to confirm the near-optimality of the proposed algorithms.

We conducted both simulation and physical experimentation to validate the proposed algorithms. The good consistency between the simulation results and the experimental results does not only suggest the physical relevance of our simulation setup, but also supports the validity of the analytical models and algorithms for the physical system. With a body length (BL) of 10 cm for the lateral line system, simulation and experimental results showed that both the GN and NR algorithms can successfully localize the dipole source and estimate its vibration amplitude and orientation within 1 BL, with the maximum localization error less than 5% of the BL. We also found that, while the GN algorithm did consistently better than the NR algorithm, the overall performance and computational complexity of the two algorithms are very comparable. We also found that the proposed algorithms showed clear advantage over the beamforming algorithm in terms of accuracy and computational efficiency. On the other hand, we note that the convergence (to the true solution) of the proposed GN and NR schemes depends on the proper choice of initial conditions, while the BF method always results in a solution that is close to the true solution, where the error is determined by the resolution of discretization in the parameter space.

The work reported in this paper will be extended in several directions. First, we used FFT to extract the signal amplitude as the sensor measurement, which is not amenable to online implementation. Our first step for future work is to use sliding discrete Fourier transform (SDFT) [34, 56] to update the signal amplitude as new raw data samples come in. This will not only allow us to perform source localization in real time, but also enable the tracking of a moving dipole source, where the received signal amplitude is time-varying. Second, we will consider a lateral line system mounted on a streamlined body (like a fish body), and accommodate the impact of the body in both the optimization of the sensor design and the development of localization algorithms.

Acknowledgments

This work was supported in part by National Science Foundation (ECCS 0547131, CCF 0820220, IIS 0916720) and Office of Naval Research (grants N000140810640, N000141210149). The authors would like to thank Hong Lei for preparing the IPMC material used in this work, and Professor Sheryl Coombs for making the mini-shaker available to us for conducting the experiments.

Appendix. Derivation of (19)

From (17), we have

$$\frac{\partial \ln P(M,\theta)}{\partial\theta} = \frac{1}{\sigma^2}\sum_{i=0}^{N-1}\left\{ -f_i(\theta)\frac{\partial f_i(\theta)}{\partial\theta} + \tanh\left(\frac{M_i f_i(\theta)}{\sigma^2}\right) M_i \frac{\partial f_i(\theta)}{\partial\theta}\right\},$$

and consequently,

$$\frac{\partial^2 \ln P(M,\theta)}{\partial\theta^2} = \frac{1}{\sigma^2}\sum_{i=0}^{N-1}\left\{ -f_i(\theta)\frac{\partial^2 f_i(\theta)}{\partial\theta^2} - \left[\frac{\partial f_i(\theta)}{\partial\theta}\right]\left[\frac{\partial f_i(\theta)}{\partial\theta}\right]^T + \tanh\left(\frac{M_i f_i(\theta)}{\sigma^2}\right) M_i \frac{\partial^2 f_i(\theta)}{\partial\theta^2} + \frac{M_i^2}{\sigma^2}\left[\frac{\partial f_i(\theta)}{\partial\theta}\right]\left[\frac{\partial f_i(\theta)}{\partial\theta}\right]^T \left[1-\tanh^2\frac{M_i f_i(\theta)}{\sigma^2}\right]\right\}. \tag{A.1}$$

Taking the negative expectation on (A.1) results in

$$-\mathbf{E}\left\{\frac{\partial^2 \ln P(M,\theta)}{\partial\theta^2}\right\} = -\frac{1}{\sigma^2}\mathbf{E}\left\{\sum_{i=0}^{N-1}\left\{ -f_i(\theta)\frac{\partial^2 f_i(\theta)}{\partial\theta^2} - \left[\frac{\partial f_i(\theta)}{\partial\theta}\right]\left[\frac{\partial f_i(\theta)}{\partial\theta}\right]^T + \tanh\left(\frac{M_i f_i(\theta)}{\sigma^2}\right) M_i \frac{\partial^2 f_i(\theta)}{\partial\theta^2} + \frac{M_i^2}{\sigma^2}\left[\frac{\partial f_i(\theta)}{\partial\theta}\right]\left[\frac{\partial f_i(\theta)}{\partial\theta}\right]^T \left[1-\tanh^2\frac{M_i f_i(\theta)}{\sigma^2}\right]\right\}\right\}$$
$$= \frac{1}{\sigma^2}\sum_{i=0}^{N-1}\left\{ f_i(\theta)\frac{\partial^2 f_i(\theta)}{\partial\theta^2} + \left[\frac{\partial f_i(\theta)}{\partial\theta}\right]\left[\frac{\partial f_i(\theta)}{\partial\theta}\right]^T - \mathbf{E}\left\{\tanh\left(\frac{M_i f_i(\theta)}{\sigma^2}\right) M_i \frac{\partial^2 f_i(\theta)}{\partial\theta^2} + \frac{M_i^2}{\sigma^2}\left[\frac{\partial f_i(\theta)}{\partial\theta}\right]\left[\frac{\partial f_i(\theta)}{\partial\theta}\right]^T \left[1-\tanh^2\frac{M_i f_i(\theta)}{\sigma^2}\right]\right\}\right\},$$

which is (19).

References

[1] Abdulsadda A T and Tan X 2011 Artificial lateral line-based localization of a dipole source with unknown vibration amplitude and direction *Proc. 15th Int. Conf. on Advanced Robotics (Tallinn, Estonia)* pp 447–52

[2] Abdulsadda A T and Tan X 2011 Underwater source localization using an IPMC-based artificial lateral line *Proc. IEEE Int. Conf. on Robotics and Automation (Shanghai, China)* pp 2719–24

[3] Abdulsadda A T and Tan X 2012 An artificial lateral line system using IPMC sensor arrays *Int. J. Smart Nano Mater.* **3** 226–42

[4] Abdulsadda A T, Zhang F and Tan X 2011 Localization of source with unknown amplitude using IPMC sensor arrays *Proc. SPIE* **7976** 797627

[5] Akanyeti O, Venturelli R, Visentin F, Chambers L, Megill W and Fiorini P 2011 What information do Ká rmá n streets offer to flow sensing? *Bioinspir. Biomim.* **6** 036001

[6] Bleckmann H 1994 *Reception of Hydrodynamic Stimuli in Aquatic and Semiaquatic Animals (Progress in Zoology)* ed W Rathmayer (Stuttgart, Germany: Gustav Fischer Verlag) pp 1–115

[7] Bleckmann H 2008 Peripheral and central processing of lateral line information *J. Comput. Physiol.* A **194** 145–58

[8] Bleckmann H, Przybilla A, Klein A, Schmitz A, Kunze S and Brucker C 2012 Station holding of trout: behavior, physiology and hydrodynamics *Nature-Inspired Fluid Mechanics* ed C Tropea and H Bleckmann (Berlin: Springer) pp 161–77

[9] Bouffanais R, Weymouth G D and Yue D K P 2011 Hydrodynamic object recognition using pressure sensing *Proc. R. Soc.* A **467** 19–38

[10] Chen X, Zhu G, Yang X, Hung D L S and Tan X 2013 Model-based estimation of flow characteristics using an ionic polymer–metal composite beam *IEEE/ASME Trans. Mechatronics* **18** 932–43

[11] Chen Z, Tan X, Will A and Ziel C 2007 A dynamic model for ionic polymer–metal composite sensors *Smart Mater. Struct.* **16** 1477–88

[12] Coombs S 2001 Smart skins: information processing by lateral line flow sensors *Auton. Robots* **11** 255–61

[13] Coombs S and Braun C B 2003 Information processing by the lateral line system *Sensory Processing in Aquatic Environments* ed S P Collin and N J Marshall (New York: Springer) pp 122–38

[14] Coombs S and Conley R A 1997 Dipole source localization by mottled sculpin: I. Approach strategies *J. Comput. Physiol.* A **180** 387–99

[15] Coombs S and Conley R A 1997 Dipole source localization by mottled sculpin: II. The role of lateral line excitation patterns *J. Comput. Physiol.* A **180** 401–15

[16] Coombs S, Hastings M and Finneran J 1996 Modeling and measuring lateral line excitation patterns to changing dipole source locations *J. Comput. Physiol.* A **178** 359–71

[17] Coombs S, Janssen J and Webb J C 1988 Diversity of lateral lne systems: evolutionary and functional considerations *Sensory Biology of Aquatic Animals* ed J Atema, R R Fay, A N Popper and W N Tavolga (New York: Springer) pp 553–94

[18] Cover T M and Thomas J A 1991 *Elements of Information Theory* (New York: Wiley)

[19] Curcic-Blake B and van Netten S M 2006 Source location encoding in the fish lateral line canal *J. Exp. Biol.* **209** 1548–59

[20] Dagamseh A M K, Lammerink T S J, Kolster M L, Bruinink C M, Wiegerink R J and Krijnen G J M 2010 Dipole-source localization using biomimetic flow-sensor arrays positioned as lateral-line system *Sensors Actuators* A **162** 355–60

[21] Dijkstra M, van Baar J J, Wiegerink R J, Lammerink T S J, de Boer J H and Krijnen G J M 2005 Artificial sensory hairs based on the flow sensitive receptor hairs of crickets *J. Micromech. Microeng.* **15** S132–8

[22] Engelmann J, Hanke W, Mogdans J and Bleckmann H 2000 Hydrodynamic stimuli and the fish lateral line *Nature* **408** 51–52

[23] Fan Z, Chen J, Zou J, Bullen D, Liu C and Delcomyn F 2002 Design and fabrication of artificial lateral line flow sensors *J. Micromech. Microeng.* **12** 655–61

[24] Fernandez V I, Maertens A, Yaul F M, Dahl J, Lang J H and Triantafyllou M S 2011 Lateral-line-inspired sensor

arrays for navigation and object identification *Mar. Technol. Soc. J.* **45** 130–46
[25] Franosch J-M P, Sichert A B, Suttner M D and van Hemmen J L 2005 Estimating position and velocity of a submerged moving object by the clawed frog *xenopus* and by fish: a cybernetic approach *Biol. Cybern.* **93** 231–8
[26] Ganley T, Hung D L S, Zhu G and Tan X 2011 Modeling and inverse compensation of temperature-dependent ionic polymer–metal composite sensor dynamics *IEEE/ASME Trans. Mechatronics* **16** 80–89
[27] Gardiner J M and Atema J 2007 Sharks need the lateral line to locate odor sources: rheotaxis and eddy chemotaxis *J. Exp. Biol.* **210** 1925–34
[28] Goulet J, Engelmann J, Chagnaud B P, Franosch J-M P, Suttner M D and van Hemmen J L 2008 Object localization through the lateral line system of fish: theory and experiment *J. Comput. Physiol.* A **194** 1–17
[29] Hassan E-S 1985 Mathematical analysis of the stimulus for the lateral line organ *Biol. Cybern.* **52** 23–36
[30] Hassan E-S 1992 Mathematical description of the stimuli to the lateral line system of fish derived from a three-dimensional flow field analysis: I. The cases of moving in open water and of gliding towards a plane surface *Biol. Cybern.* **66** 443–52
[31] Hassan E-S 1992 Mathematical description of the stimuli to the lateral line system of fish derived from a three-dimensional flow field analysis: II. The case of gliding alongside or above a plane surface *Biol. Cybern.* **66** 453–61
[32] Hassan E-S 1993 Mathematical description of the stimuli to the lateral line system of fish derived from a three-dimensional flow field analysis: III. The case of an oscillating sphere near the fish *Biol. Cybern.* **69** 525–38
[33] Hoekstra D and Janssen J 1985 Non-visual feeding behavior of the mottled sculpin, *cottus bairdi* in Lake Michigan *Environ. Biol. Fishes* **12** 111–7
[34] Jacobsen E and Lyons R 2003 The sliding DFT *IEEE Signal Process. Mag.* **20** 74–80
[35] Kalmijn A J 1988 Hydrodynamic and acoustic field detection *Sensory Biology of Aquatic Animals* ed J Atema, R R Fay, A N Popper and W N Tavolga (New York: Springer) pp 83–130
[36] Kay S M 1993 *Fundamentals of Statistical Signal Processing: Estimation Theory* (Upper Saddle River, NJ: Prentice-Hall)
[37] Kim K J and Shahinpoor M 2003 Ionic polymer–metal composites: II. Manufacturing techniques *Smart Mater. Struct.* **12** 65–79
[38] Klein A and Bleckmann H 2011 Determination of object position, vortex shedding frequency and flow velocity using artificial lateral line canals *Beilstein J. Nanotechnol.* **2** 276–83
[39] Kroese A B A and Schellart N A M 1992 Velocity- and acceleration-sensitive units in the trunk lateral line of the trout *J. Neurophysiol.* **68** 2212–21
[40] Lamb H 1932 *Hydrodynamics* (Cambridge: Cambridge University Press)
[41] Liao J C 2004 Neuromuscular control of trout swimming in a vortex street: implications for energy economy during the Kármán gait *J. Exp. Biol.* **207** 3495–506
[42] Liu C 2007 Micromachined biomimetic artificial haircell sensors *Bioinspir. Biomim.* **2** S162–9
[43] McConney M E, Chen N, Lu D, Hu H A, Coombs S, Liu C and Tsukruk V V 2009 Biologically inspired design of hydrogel-capped hair sensors for enhanced underwater flow detection *Soft Matter* **5** 292–5
[44] McHenry M J, Strother J A and van Netten S M 2008 Mechanical filtering by the boundary layer and fluid–structure interaction in the superficial neuromast of the fish lateral line system *J. Comput. Physiol.* A **194** 795–810
[45] Montgomery J C, Baker C F and Carton A G 1997 The lateral line can mediate rheotaxis in fish *Nature* **389** 960–3
[46] Oppenheim A V and Schafer R W 2010 *Discrete-Time Signal Processing* 3rd edn (Upper Saddle River, NJ: Pearson)
[47] Ozaki Y, Ohyama T, Yasuda T and Shimoyama I 2000 An air flow sensor modeled on wind receptor hairs of insects *Proc. 13th IEEE Int. Conf. on Micro Electro Mechanical Systems (Miyazaki, Japan)* pp 531–6
[48] Pandya S, Yang Y, Jones D L, Engel J and Liu C 2006 Multisensor processing algorithms for underwater dipole localization and tracking using MEMS artificial lateral-line sensors *EURASIP J. Appl. Signal Process.* **2006** 76593
[49] Pitcher T J, Partridge B L and Wardle C S 1976 A blind fish can school *Science* **194** 963–5
[50] Pohlmann K, Atema J and Breithaupt T 2004 The importance of the lateral line in nocturnal predation of piscivorous catfish *J. Exp. Biol.* **207** 2971–8
[51] Qualtieri A, Rizzi F, Todaro M T, Passaseo A, Cingolani R and De Vittorio M 2011 Stress-driven AlN cantilever-based flow sensor for fish lateral line system *Microelectron. Eng.* **88** 2376–8
[52] Ren Z and Mohseni K 2012 A model of the lateral line of fish for vortex sensing *Bioinspir. Biomim.* **7** 036016
[53] Sadeghi M M, Peterson R L and Najafi K 2011 Micro-hydraulic structure for high performance bio-mimetic air flow sensor arrays *Proc. IEEE Int. Electron Devices Meeting* pp 29.4.1–29.4.4
[54] Sarles S A, Pinto P and Leo D J 2011 Hair cell sensing with encapsulated interface bilayers *Proc. SPIE* **7975** 797509
[55] Shahinpoor M and Kim K 2001 Ionic polymer–metal composites: I. fundamentals *Smart Mater. Struct.* **10** 819–33
[56] Shatara S and Tan X 2010 An efficient, time-of-flight-based underwater acoustic ranging system for small robotic fish *IEEE J. Ocean. Eng.* **35** 837–46
[57] Sichert A B, Bamler R and van Hemmen J L 2009 Hydrodynamic object recognition: when multipoles count *Phys. Rev. Lett.* **102** 058104
[58] Sichert A B and van Hemmen J L 2010 How stimulus shape affects lateral-line perception: analytical approach to analyze natural stimuli characteristics *Biol. Cybern.* **102** 177–80
[59] Venturelli R, Akanyeti O, Visentin F, Jezov J, Chambers L D, Toming G, Brown J, Kruusmaa M, Megill W M and Fiorini P 2012 Hydrodynamic pressure sensing with an artificial lateral line in steady and unsteady flows *Bioinspir. Biomim.* **7** 036004
[60] von Campenhausen C, Riess I and Weissert R 1981 Detection of stationary objects by the blind cave fish *Anoptichthys jordani* (characidae) *J. Comput. Physiol.* **143** 369–74
[61] Wang Y, Lee C and Chiang C 2007 A MEMS-based air flow sensor with a free-standing microcantilever structure *Sensors* **7** 2389–401
[62] Windsor S P, Tan D and Montgomery J C 2008 Swimming kinematics and hydrodynamic imaging in the blind Mexican cave fish (*astyanax fasciatus*) *J. Exp. Biol.* **211** 2950–9
[63] Yang Y, Chen J, Engel J, Pandya S, Chen N, Tucker C, Coombs S, Jones D L and Liu C 2006 Distant touch hydrodynamic imaging with an artificial lateral line *Proc. the Natl Acad. Sci. USA* **103** 18891–5
[64] Yang Y, Klein A, Bleckmann H and Liu C 2011 Artificial lateral line canal for hydrodynamic detection *Appl. Phys. Lett.* **99** 023701
[65] Yang Y, Nguyen N, Chen N, Lockwood M, Tucker C, Hu H, Bleckmann H, Liu C and Jones D L 2010 Artificial lateral line with biomimetic neuromasts to emulate fish sensing *Bioinspir. Biomim.* **5** 016001